Comparison of computational water models for simulation of calcium–silicate–hydrate

Qing Ji [a], Roland J.-M. Pellenq [b,c], Krystyn J. Van Vliet [a,*]

[a] Department of Materials Science and Engineering, Massachusetts Institute of Technology, 77 Massachusetts Avenue, Cambridge, MA 02139, USA
[b] Department of Civil and Environmental Engineering, Massachusetts Institute of Technology, 77 Massachusetts Avenue, Cambridge, MA 02139, USA
[c] Centre Interdisciplinaire des Nanosciences de Marseille, CNRS- U. Marseille, Campus de Luminy, 13288, Cedex 09, Marseille, France

ABSTRACT

Calcium silicate hydrate, or C–S–H, is the chief hydration product of Portland cement. The structure of the C–S–H phase within cement has been proposed and developed via molecular simulations. In such simulations, empirical interatomic potentials for water molecules within C–S–H are adopted to govern the position and relative motion of this key constituent. Initial simulations and force fields of C–S–H have assumed the simplest molecular model of H_2O termed "single point charge" or SPC, but this choice has not been validated by comparison with other computational models of water that confer additional bond flexibility or charge distribution. To enable efficiently computational modeling of C–S–H and to explore the role that H_2O plays in maintaining C–S–H structure and properties, the choice of an efficient and accurate water model is critical. Here, we consider five distinct, classical atomistic water models (SPC, TIP3P, TIP4P, TIP4P05, and TIP5P) to determine the effects of these computational simplifications on C–S–H properties. Quantitative comparison of all five water models shows that the appropriate water model depends on the C–S–H characteristics of interest. Among these models, both SPC and TIP5P models successfully predict key properties of the structure and elastic constants of C–S–H, as well as the dynamics of water molecules within C–S–H.

© 2011 Elsevier B.V. All rights reserved.

1. Introduction

Calcium–silicate–hydrate (termed C–S–H) is the chief reaction product resulting from hydration of silicate phases in Portland cement. Thus, the formation and properties of this key nanogranular gel in cementitious materials is defined largely by water. Further, the nanostructure of the hardened cement paste, and the environmental changes in those properties during shrinkage or creep, are affected significantly by changes in water content [1].

Although the experimental research on cement has been developed over centuries [2], our understanding of nanoscale C–S–H within such composite materials is relatively limited and recent. In 2006, Bordallo et al. used quasielastic neutron scattering (QENS) to differentiate the water within hardened cement pastes into three classes: water molecules that are chemically or strongly bound to and are integral to the C–S–H structure; that are physically bound to and interact with the surface of the gel pores in the paste; and that are unbound and simply confined within the larger capillary pores of cement paste [3]. Only the dynamics of the water within the gel pores and capillary pores were accessed by QENS, and thus comparatively little is known about the chemically bound or "structural

water" that stabilizes and comprises the structure of C–S–H. In 2007, Allen et al. proposed the average water content in C–S–H by combining small-angle neutron and X-ray scattering data, and by exploiting the hydrogen/deuterium neutron isotope effect [4]. However, validation of such hypotheses and access to water structure and dynamics via experiments alone is obfuscated by challenges with both material purity and instrument resolution at the relevant length- and timescales [5,6].

Molecular scale simulations provide complementary means to consider the structure, properties, and dynamics of nanoscale C–S–H. A molecular model of C–S–H that is consistent with experimental signatures of this nanoscale phase was reported by Pellenq et al. [7]. This model was obtained via introduction of defects within tobermorite-like structures, and computational hydration of those defected structures to obtain reasonable agreement with physical, structural, and mechanical experiments for this phase [4]. Molecular scale simulations that can define the signatures of this water within C–S–H are enabled by such models, and can aid in the design of science-driven experiments.

However, the selection or development of molecular water models within such simulations is nontrivial. Water molecules exhibit a strong dipole moment and a complex phase diagram [8–14]. The first water model was proposed by Bernal and Fowler and benchmarked against measured vibrational energy levels of water

---

* Corresponding author. Tel.: +1 617 253 3315; fax: +1 617 253 8745.
  E-mail address: krystyn@mit.edu (K.J. Van Vliet).

[15]. Following this achievement, water models abound: more than 50 distinct, classic models of this phase have been published [16]. Each such model assumes different levels of simplification regarding charge, flexibility, and other characteristics of each classical water molecule. As implied by many reviews, the ideal water model is still in progress; general surveys of existing water models are typically conducted for each material and each property of interest [16,17].

In order to enable efficiently computational modeling of C–S–H and to explore the role that H_2O plays in maintaining C–S–H structure and properties, the choice of an efficient and accurate water model is critical. Here, we consider five distinct, classical atomistic water models (termed historically as single point charge or SPC [18], transferable intermolecular potential or TIP3P [19], TIP4P [20], TIP4P05 [21], and TIP5P [22]) and rigorously compare the resulting C–S–H structure, dynamics, and mechanical properties.

2. Simulation model and methods

2.1. Calcium–silicate–hydrate model

An equilibrated structure of the C–S–H atomistic unit cell for a specific composition of $(CaO)_{1.65}(SiO_2)(H_2O)_{1.63}$ was obtained from the related development of a classical force field for C–S–H, termed C–S–H-FF [23]. This calcium–silicate–hydrate unit cell can be described as two layers of calcium- and silicon-rich regions, separated by water-rich regions (Fig. 1b). In fact, there exist water molecules within the Ca- and Si-rich regions (intralayer water) and between those regions (interlayer water). The electrostatic charge in the structure is balanced by that of the oxygen ions.

The potential energy function adopted in this study to govern interatomic interactions includes four components: harmonic bond stretching $E_{bondstretch\ ij} = 0.5 \times k_b \times (r_{ij} - r_0)^2$, harmonic angle bending $E_{anglebend\ ijk} = 0.5 \times k_\theta \times (\theta_{ijk} - \theta_0)^2$, Coulombic interactions $E_{Coul} = \frac{e^2}{4\pi\varepsilon_0} \sum_{i \neq j} \frac{q_i q_j}{r_{ij}}$ and Lennard–Jones potential $E_{VDW} = \sum_{i \neq j} \left[\frac{C_{12}}{r_{ij}^{12}} - \frac{C_6}{r_{ij}^6} \right]$ for the dispersion–repulsion interactions. Here, k_b is a force constant and r_o represents the equilibrium bond length; r_{ij} is inter-atom distance; k_θ is a force constant and θ_o represents the equilibrium angle; q_i and q_j are partial charges; e is the charge of the electron; and ε_0 is the dielectric permittivity of vacuum (8.85419×10^{-12} F/m). The Lennard–Jones parameters C_{12} and C_6 depend on the pairs of atom types. The magnitudes of these interaction parameters were adopted as those developed for C–S–H-FF [23] and were validated against both ab initio (density functional theory) calculations and experimental data on crystalline tobermorite.

We considered five classical atomistic water models: SPC [18], TIP3P [19], TIP4P [20], TIP4P05 [21] and TIP5P [22]; the differences in molecular representation of atomic positions and charge are indicated in Fig. 1a. The interaction potential parameters for the five water models are shown in Table 1. With the exception of TIP5P, all the models were set as flexible (i.e., bond stretch and angle distortion resistance were indicated by finite stiffness, rather than rigidly maintained) [22]. The differences among the five classical water models reported here can be summarized by three aspects. First, the equilibrium O–H bond length and H–O–H angles are shorter and more acute, respectively, for TIP models as compared to the SPC model. Second, charge distributions in these five models are identical, but the representation of this charge distribution differs: SPC and TIP3P place this negative charge on the oxygen atom; TIP4P and TIP4P05 place one negative charge sites at a dummy atom and TIP5P instead places two negative charge sites at two dummy atoms. Third, the Lennard–Jones (LJ) parameters differ slightly due to the different properties used to fit these
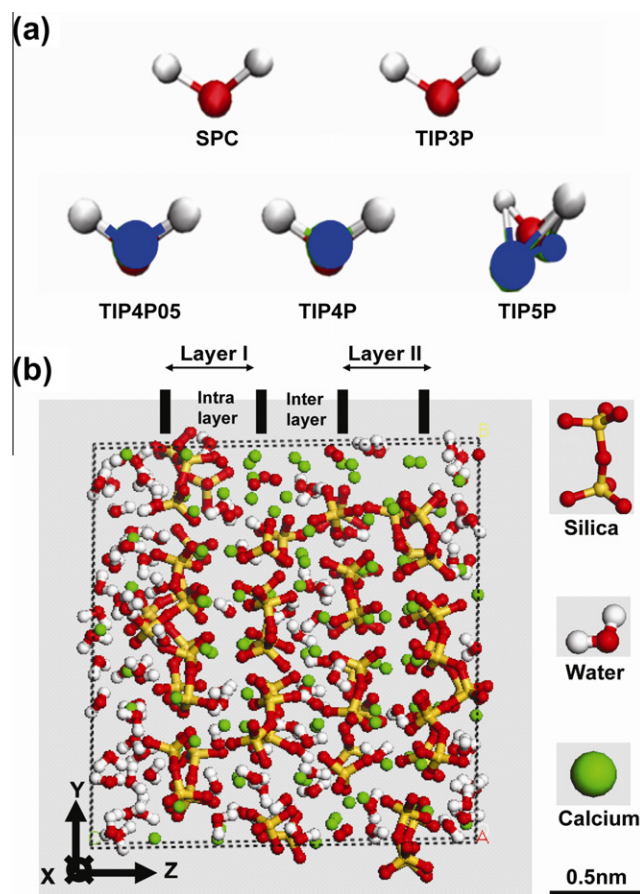

Fig. 1. Schematics of (a) five water models and (b) calcium–silicate–hydrate (C–S–H) unit cell. In (a), white spheres correspond to hydrogen atoms; red to oxygen atoms and blue to dummy atoms that hold the negative charge. In (b), gold chains are silica chains, green spheres are calcium ions; and red and white spheres are oxygen and hydrogen atoms in water molecules, respectively. The C–S–H unit cell $[(CaO)_{1.65}(SiO_2)(H_2O)_{1.63}]$ is described as two layers of calcium- and silicon-rich regions (intralayer) separated by water-rich regions (interlayer). Both the water molecules and calcium atoms exist in the intralayer and interlayer regions.

parameters for these different water models [16]. For comparisons of these water models within the C–S–H structure, the number and position of water molecules within the equilibrated structure were initially identical, and were realized by substituting TIP water molecules at the same oxygen atom coordinate positions as used for the SPC model.

2.2. Simulation methods

All simulations reported here were conducted using a large-scale atomic/molecular massively parallel simulator, GROMACS [24,25]. The initial C–S–H unit cell (Fig. 1b) was energy minimized via the conjugate gradient algorithm; the unit cell density was equilibrated at constant pressure (NPT ensemble, 50 ns), followed by the constant volume NVT ensemble (20 ns, to collect equilibrated data efficiently). In the last 10 ns of this trajectories, data were collected and analyzed at intervals of 1 ps. Temperature was maintained at 300 K by the Nosé–Hoover method, and pressure coupling achieved via the Parrinello–Rahman algorithm to allow for changes in on both unit cell box lengths and angles. Time steps for integrations were 0.1 fs and 2 fs for NPT and NVT trajectories, respectively. Coulombic interactions were evaluated using the Ewald summation technique, and the Lennard–Jones interaction was summed within a prescribed cutoff radius R_{max} of ~1.1 nm. This cutoff radius approximates that reported previously

Table 1
Interaction potential parameters of the five classical molecular water models considered. Parameters b_0 and θ_0 are the equilibrium values of bond length and angle, respectively; k_b and k_θ are harmonic force constants; C_6 and C_{12} are Lennard–Jones prefactor parameters, and q_H corresponds to the positive charge on the hydrogen atom.

Parameters							
Model	b_0 (nm)	k_b (kJ/nm^2)	θ_0 (°)	k_θ (kJ/o^2)	C_6 (kJ-nm^6)	C_{12} (kJ-nm^{12})	q_H (e)
SPC	0.1	463811	109.47	383.1	2.58E−03	2.58E−06	0.41
TIP3P	0.09572	502416	104.52	628.02	2.49E−03	2.44E−06	0.417
TIP4P05	0.09572	502416	104.52	628.02	3.08E−03	3.06E−06	0.5564
TIP4P	0.09572	502416	104.52	628.02	2.55E−03	2.51E−06	0.52
TIP5P	0.09572	–	104.52	–	2.47E−03	2.28E−06	0.241

for C–S–H simulations that utilized a core–shell potential (~1.2 nm) [7], and met the GROMACS requirement of cutoff radius less than half the unit cell length [24,25].

Calculation of elastic constants for each of these five C–S–H models was obtained using the box deformation method. Deformation in uniaxial tension and simple shear was imposed in 12 separate simulations for each model. The maximum imposed strain was 0.006, with strain increments of 0.001, and the strained structures were relaxed via conjugate gradient minimization prior to calculation of elastic constants. This calculation method was taken from previous study of nano-single crystal of nickel [26]. Elastic constants C_{ij} were calculated from virial stress–strain relations obtained from the above unit cell deformations [27,28].

3. Results and discussion

Here we investigated the dependency of several properties of C–S–H on the choice of computational water model, as well as the relative accuracy and computational efficiency among these models. These results are reported in terms of structure, dynamics, and mechanics, and are compared with available experiments and previous computational simulations.

3.1. Structure

The structure of C–S–H is notoriously complex, nanogranular, and dependent on both environment and hydration time [1,29–31]. The C–S–H structure used herein was constructed by adsorption of water molecules via Grand Canonical Monte Carlo simulations as the previous study [7]. The final hydrated C–S–H composition was found to be $(CaO)_{1.65}(SiO_2)(H_2O)_{1.63}$, in reasonable agreement with experiments [4,7]. Here, we compare the C–S–H structure among these water models in terms of unit cell dimensions, physical density, and X-ray spectra.

Fig. 2a compares the unit cell dimensions of C–S–H for different water models with previous atomistic simulations that adopted a comparatively expensive core–shell potential [7]. Unit cell lengths are within ~0.1 nm and unit cell angles are within ~4° of the literature [7]. This indicates that the unit cell dimensions are insensitive to water model. To compare models quantitatively, we calculated the averaged relative errors of the three unit cell lengths and three unit cell angles; TIP5P exhibits the smallest error (1.5%), but all models reproduce this unit cell within <3% error. To our knowledge, no related experimental data are available.

Densities of these five C–S–H unit cells with different water models are shown in Fig. 2b, and ranged from 2.46 to 2.49 g/cm^3. Adsorption experiments (of helium, water and methanol) indicate the density of a similar C–S–H composition ($C_{1.7}SH_{1.5}$) to range 2.45–2.8 g/cm^3 [29,32]. Therefore, all calculated densities were well within this experimental range. To compute relative error, a reference density 2.6 g/cm^3 was adopted as a conservative estimate at the midpoint of this range, as well as the approximate density of the previously simulated C–S–H [7]. The relative error was smallest for TIP4P water (4.2%).

The presence of long-range and short-range order can be measured experimentally by several methods including X-ray [33]. Here the powder diffraction patterns of X-ray were calculated and compared to available experimental data for C–S–H (Fig. 2c). Calculated diffraction spectra were determined via the powder pattern function (Mercury, Cambridge Crystallographic Data Centre) at wavelength λ = 0.154 nm according to the reported experimental settings of the instrumentation [34,35]. Two major diffraction peaks are located around 2θ = 7° and 2θ = 30°; representing characteristic distances of 1.1 and 0.3 nm, respectively. The first peak at 2θ = 7° represents the interlayer distance of C–S–H (~1.1 nm) [7]. As shown in Fig. 2c, all models display a sharp peak at approximately the same angle, indicating that the interlayer distance in C–S–H is insensitive to the choice of water model. The second peak at 2θ = 30° represents the interatomic distances. This peak is broader than the first, and can be attributed to the short-range order of C–S–H. The angles of these intensity peaks compare well with the experimental data for calcium (alumino-)silicate hydrate (Al–C–S–H) [36]. The full widths at half-maximum (FWHM) of the peak are shown for both experimental data and our simulation results. The FWHM of the experiment is ~2.5°, while those for simulation are ~5°. This implies that the simulated structures are more amorphous than that in experiment, and may be attributed in part to the significant aluminum impurities in the experimental sample. Among the five models, TIP3P shows the relative narrow peak with a relative error of 76.4%, while TIP4P has the broadest peak with a relative error of 147.6%, with respect to experiments. The relatively large error produced by TIP4P is probably due to the failure of TIP4P to yield correct dielectric constant, which is significant for the ion-composed C–S–H. As Rick and Vega examined, the lower value of the dielectric constant ε = 50 for TIP4P models is a direct consequence of the higher quadrupole moment of this type of model [37,38]. Thus, TIP3P is more accurate in predicting the experimentally reported structural atom pair characteristics of C–S–H.

3.2. Dynamics

The dynamics of water within cement ranges over multiple length- and timescales, and significantly affects processes ranging from nanoscale hydration to macroscale shrinkage. In particular, the conditions under which water molecules move within the confined, multiscale pores of cement are of practical importance; water dynamics within the nanoscale C–S–H is less accessible to experiments, but is intimately related to water dynamics among C–S–H particles within the cement pastes. Here, we compare the molecular-scale vibrations and mobility of water within the C–S–H phase as a function of water model, and compare these data with available experiments.

Fig. 3a summarizes simulated mid-infrared (IR) spectra and compares these with experimental data [39]. The IR spectra were calculated via the VMD 1.8.7 IR spectral density calculator [40]. Note that the experimental data for synthetic C–S–H with Ca/Si = 1.7 indicate four peaks at ~650, ~1200, ~1600 and ~3600 cm^{-1}. These

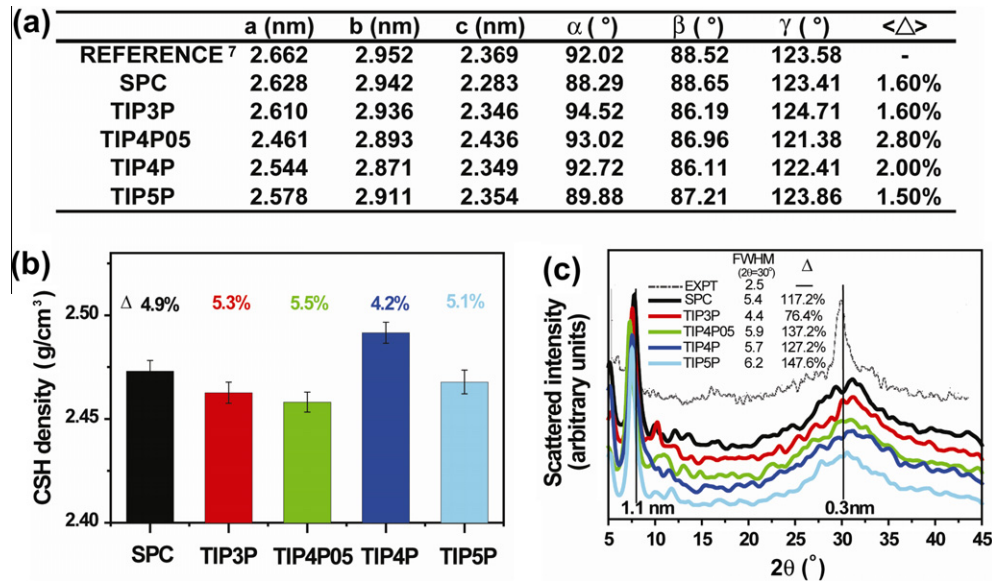| (a)	a (nm)	b (nm)	c (nm)	α (°)	β (°)	γ (°)	⟨△⟩
REFERENCE[7]	2.662	2.952	2.369	92.02	88.52	123.58	-
SPC	2.628	2.942	2.283	88.29	88.65	123.41	1.60%
TIP3P	2.610	2.936	2.346	94.52	86.19	124.71	1.60%
TIP4P05	2.461	2.893	2.436	93.02	86.96	121.38	2.80%
TIP4P	2.544	2.871	2.349	92.72	86.11	122.41	2.00%
TIP5P	2.578	2.911	2.354	89.88	87.21	123.86	1.50%

Fig. 2. Comparison of C–S–H structural characteristics. (a) Unit cell dimensions, where a, b, and c are the unit cell lengths and α, β, and γ are the inclination angles. ⟨△⟩ Denotes the average relative error with respect to the unit cell of the core–shell model for this same composition of C–S–H [7]. (b) C–S–H density. Error bars indicate standard deviation among 50,000 configurations over the last 5 ns of the NPT trajectory of molecular dynamics simulations. △ denotes relative error with respect to the average experimentally reported density of 2.6 g/cm³ [29]. (c) X-ray diffraction spectra, including powder diffraction experiments [36]. The first peak (~7°) corresponds to the interlayer distance of 1.1 nm, and is well predicted in simulation for all five models. The second peak (~30°) corresponds to intermolecular distance of 0.3 nm, and is broader in simulations. Peak full width at half-maximum at $2\theta = 30°$ (FWHM) is shown, and △ denotes relative errors with respect to the experimental peak width of ~2.5°.
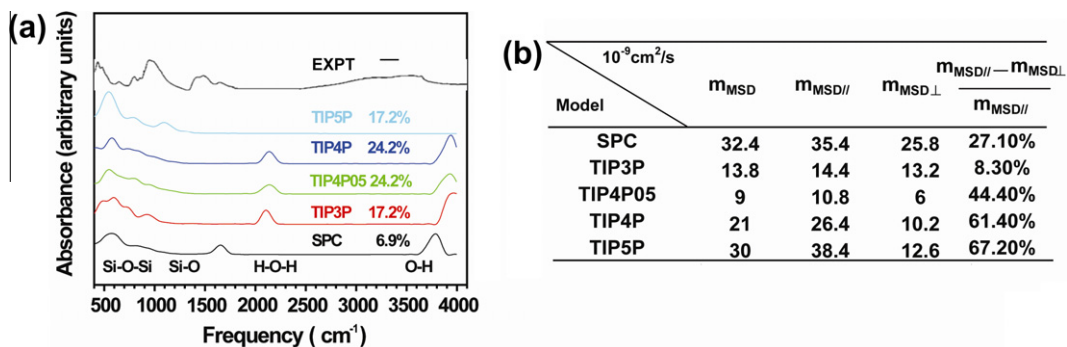

Fig. 3. Comparison of C–S–H dynamic characteristics. (a) Infrared absorption spectrum from experiment [39] and simulation. Peaks are related to specific bending angles and bond stretching as follows: ~500 cm^{-1} corresponds to the bending angle of Si–O–Si; ~1000 cm^{-1} corresponds to the stretching of Si–O bonds; ~1500 cm^{-1} corresponds to the bending angle of H–O–H; ~3600 cm^{-1} corresponds to the stretching of O–H bonds. The denoted percentage is the average relative error with respect to the frequency of these four experimental peaks. (b) Mean squared displacement of water molecules, where m_{MSD} corresponds to the average slope over molecular dynamics trajectories. $m_{MSD\perp}$ and $m_{MSD\parallel}$ correspond to the slope of the displacement in the direction perpendicular to and parallel to silicate rich layers in C–S–H, respectively, and the last column indicates displacement anisotropy with respect to those directions.

represent the vibrations related to Si–O–Si bending, Si–O stretching, H–O–H bending, and O–H stretching, respectively. Although water model-dependence on Si–O interactions is expected to be weak, the Colulombic (nonbonded) nature of the Si–O interaction could possibly be perturbed by changes in hydrogen bonding interactions between the Si–O bond and H$_2$O; our calculations explore this possibility.

Among these vibrational peaks, Si–O–Si bending was reproduced well in all five water models. Two of the four peaks (H–O–H bending and H–O stretching) were well reproduced with the SPC water model. In contrast, TIP3P, TIP4P and TIP4P05 water models exhibited peaks at higher frequencies than those of experimental data. Finally, TIP5P did not exhibit any absorption peaks at these higher frequencies due to the fixed bond lengths and angles in this water model. However, only the TIP5P model produced a (weak) peak at ~1100 cm^{-1} indicative of Si–O stretching. Therefore, we can conclude that Si–O–Si interactions are independent of the choice of water model, whereas Si–O bond stretching depends slightly on this choice. The average relative errors of the frequencies of these four peaks are shown in Fig. 3, as compared with experiments. The SPC model produces an average error among these peak frequencies of only 6.9%. Thus, if the property of interest is the vibration of water itself (within the C–S–H), SPC more accurately simulates the H–O–H and O–H vibrations of the confined water molecules; if the property of interest is instead the vibration of Si–O bonds, TIP5P is a better choice.

In this study, the relative ease of water mobility within C–S–H was characterized by the slope of the mean square displacement m_{MSD}. This quantity is of course related to diffusivity, but is not equated with diffusivity here because water molecules do not exhibit displacements consistent with the Einstein diffusion relation over the analyzed conditions and timescales. As shown in Fig. 3b, m_{MSD} ranges from 9 to 32 × 10^{-9} cm^2/s for water within C–S–H, depending on the choice of water representation. Note that the

mobility of bulk water for all of these computational models exceeds these values by four order of magnitude [41,42]. This severe decrease in relative motion of water is attributable to the extreme confinement condition of C–S–H, as noted by Kalinichev et al. [43]. Under such an extremely small confinement, the observed m_{MSD} in the present study are in good agreement with previous reports from Bejaoui and Kamali-Bernard [44,45].

Although the C–S–H unit cell does not exhibit well-defined pores, the silicate-rich interlayer distance is ~0.6 nm and the intralayer distance is 0.4 nm. To our knowledge, however, there are no experiments reporting the mean-squared-displacement of water within C–S–H grains, but rather within pores separating the C–S–H grains comprising cement pastes [3]. However, several groups have noted that the C–S–H phase is anisotropic in its structure [46,47]. Therefore, we compared these water models on the basis of anisotropic mobility, parallel to and perpendicular to the silicate-rich layers.

Fig. 3b shows that this mobility is greater parallel to the silicate layers as compared to perpendicular to those layers, as expected. Further, the degree of anisotropic mobility varies with respect to the details of each water model, ranging from 8% (TIP3P) to 67% (TIP5P). For TIP4P water, Lee et al. and Giovanbattista et al. have reported similarly anisotropic displacement of the water confined between two flat silica surfaces [48,49]. However, those simulations exhibited only 11% anisotropy in silica slits, as compared to the 61% anisotropy we find for the integral TIP4P water confined within the C–S–H structure. Therefore both the choice of water model and the level of confinement should be considered in evaluations of the anisotropic water mobility. Here, we note that TIP5P water confers the greatest degree of anisotropy to this water mobility within C–S–H; however, the anisotropy of water mobility within C–S–H remains to be verified experimentally.

3.3. Mechanics

Cement and concrete applications are largely defined by the mechanical properties of these composites in the hardened state. The elastic and plastic properties of the C–S–H phases will plausibly contribute to those of the macroscale pastes and composites; investigations of such experimental correlations are ongoing. Our present simulations compute the elastic properties such as E and ν (Young's elastic modulus and Poisson's ratio, respectively) of the fully dense, or monolithic, C–S–H. These properties can be extrapolated from experiments on C–S–H of variable packing density, but not measured directly for individual nanoscale C–S–H grains [4,50], In contrast, elastic properties of C–S–H phases of varying packing density have been reported experimentally, including the average indentation modulus m that is defined as $E/(1-\nu^2)$ for each packing density-defined phase (e.g., low density or high density C–S–H), and the indentation modulus of the monolithic C–S–H phase M that is extrapolated from experiments to a packing density $\eta = 1$ [51,52]. These experimentally accessible properties can be inferred from simulations by assuming a specific packing density $\eta = 1$ for monolithic C–S–H with M, and $\eta < 1$ for assumptions of finite granular packing with m. Thus, we compared the elastic constant matrix C_{ij} of monolithic C–S–H computed using each water model with previous instrumented nanoindentation experimental studies on hardened cement pastes that directly measured m or extrapolated M.

Fig. 4a summarizes the computed C_{ij} of C–S–H obtained using the five water models. For each water model, standard deviation of each element in the matrix was calculated among ten configurations (differing slightly in atomic positions) obtained in the last 10 ns of the NVT trajectories. The corresponding confidence interval represents approximately 5% of the mean elastic constants obtained through a more computationally expensive core–shell model simulation [7];

this confidence interval of 5% is comparable to the experimental measurement error for elastic properties [51,53].

To compare quantitatively the computed elastic constants on the basis of the entire C_{ij} matrix, two mathematical parameters were considered: Euclidean and Riemannian distances. Both approaches quantify the distance between two matrices [23], with a smaller distance implying closer agreement with the reference dataset. Fig. 4a shows that all five water models exhibit differences of less than 2%, as compared to a reference calculation of identical composition computed via the core–shell representation of all atoms within C–S–H including the water molecules [7]. On this basis, although the difference in elastic constants among all water models is quite modest, the best agreement with previous simulations that account for water molecule polarization is TIP4P05 water. To compare with experimental reports for C–S–H elastic properties, the indentation modulus M of the fully dense C–S–H was computed from the bulk modulus K and shear modulus G based on the C_{ij} matrix in Fig. 4a, as $M = 4G \times \frac{3K+G}{3K+4G}$. These M were compared to Ulm et al's reports that extrapolated M from instrumented indentation experiments on real cement pastes of variable packing density η, via a linear scaling self-consistent model to the limit $\eta = 1$ [50,54]. Fig. 4b shows that most water models considered overestimated M with respect to this experimental extrapolation by ~12%, with TIP4P giving the largest difference of ~20%. Alternatively, our simulations can be related directly to the experimental measurements in the absence of such extrapolation, if we instead assume and impose a finite packing density to calculate m for a porous medium of $\eta = 0.65$ (i.e., low density C–S–H) [7,51,52,55]. Fig. 4c shows that SPC, TIP3P, TIP4P05 and TIP5P water models exhibited a relative error in indentation modulus of low density C–S–H m of ~11%, with TIP4P again yielding the largest deviation of 18.6%. However, the confidence interval of the indentation modulus measured for C–S–H regions in hardened cement pastes is typically ~10% [51]. Thus, most of the water models considered herein predict elastic properties with approximately the same accuracy. However, the SPC model exhibits the best agreement with experiment. In summary, TIP4P05 water best captures elastic anisotropy at the details of the elastic constant matrix, and SPC water best predicts the isotropic elastic moduli inferred from instrumented indentation-based experiments.

3.4. Summary of comparisons

Table 2 summarizes the percentage error obtained for each water model, in terms of each structural, dynamic, and mechanical property of C–S–H considered herein. Each property was compared with experiments when available, and with previous simulations using a more computationally expensive water potential when experiments were not available. To compare these models in a manner that enables one to identify potentially superior water models quantitatively, the average error among all such properties is also reported. The final result is that SPC and TIP5P exhibited the lowest average error of 36.1% and 36.3% respectively, and that TIP4P05 exhibited the greatest average error of 38.7%. For most properties considered here, the flexible SPC water model agreed best with previous predictions or measurements. Among these models, SPC water showed the lowest level of anisotropy in water mobility, but we noted that this characteristic has not yet been reported experimentally. Although TIP5P water showed the similar level of average agreement with previous calculations, a further advantage of flexible SPC is its computational efficiency. Specifically, the real time required for identical molecular dynamics simulations of C–S–H with SPC water is 50% shorter than that required of TIP5P water (e.g., 20 ns NVT simulation run times of 7 h 21 min and 12 h 26 min, respectively, for parallelized calculations on 8 nodes of 2.66 GHz processors in the GROMACS compute engine for 2016 atoms). Thus, if general accuracy of C–S–H properties is required and computational efficiency is a competing concern,
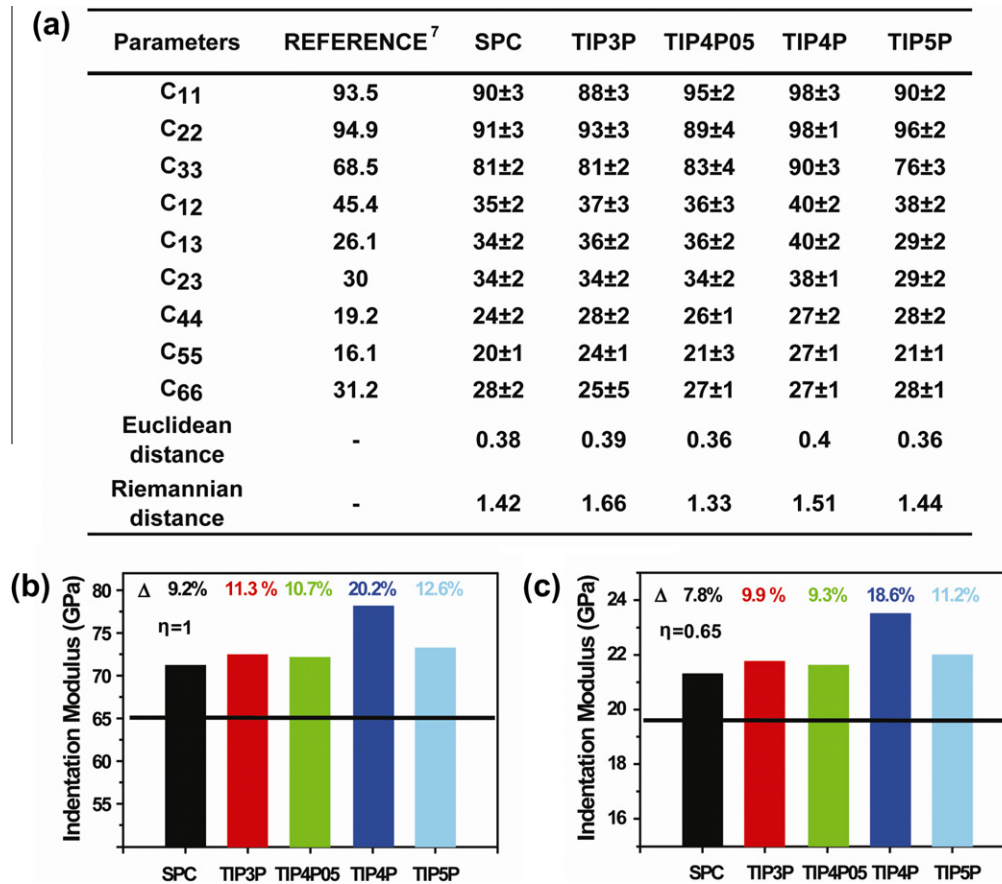
Parameters	REFERENCE[7]	SPC	TIP3P	TIP4P05	TIP4P	TIP5P
C_{11}	93.5	90±3	88±3	95±2	98±3	90±2
C_{22}	94.9	91±3	93±3	89±4	98±1	96±2
C_{33}	68.5	81±2	81±2	83±4	90±3	76±3
C_{12}	45.4	35±2	37±3	36±3	40±2	38±2
C_{13}	26.1	34±2	36±2	36±2	40±2	29±2
C_{23}	30	34±2	34±2	34±2	38±1	29±2
C_{44}	19.2	24±2	28±2	26±1	27±2	28±2
C_{55}	16.1	20±1	24±1	21±3	27±1	21±1
C_{66}	31.2	28±2	25±5	27±1	27±1	28±1
Euclidean distance	-	0.38	0.39	0.36	0.4	0.36
Riemannian distance	-	1.42	1.66	1.33	1.51	1.44

Fig. 4. Comparison of C–S–H elastic properties. (a) Elastic constants and the relative Euclidean and Riemannian difference among the five water models. Referenced elastic constants are taken from previously reported simulations of the same structure that utilized a more computationally expensive core–shell representation of atomic interactions [7]. All elastic constants are reported in units of GPa. Error is reported as the standard deviation of ten configurations in last 10 ns NVT with interval 1 ns. Euclidean and Riemannian differences enable comparison among elastic constant matrices [23]. (b) Computed indentation elastic modulus $M = E/(1-v^2)$ for C–S–H, where the horizontal line indicates that extrapolated from instrumented indentation experiments to with a C–S–H packing density $\eta = 1$ (65 GPa). (c) Computed indentation elastic modulus m assuming a finite packing density of $\eta = 0.65$, which is that reported previously for instrumented nanoindentation experiments sampling regions of low-density C–S–H of composite indentation modulus $m = 19.75$ (GPa) [7,51]. Δ indicates average relative error with respect to these experimental values.

Table 2
Comparison among water models in terms of structure, dynamics and elastic constant. The listed percentages are relative errors with different criteria for each water model. The last row shows the average value of all errors. The smaller average error indicates a better performance.

	Criterion	SPC (%)	TIP3P (%)	TIP4P05 (%)	TIP4P (%)	TIP5P (%)
Density	2.6 g/cm^2	4.9	5.3	5.5	4.2	5.1
X-ray	Experimental FWHM$_{2\theta=30°}$	117.2	76.4	137.2	127.2	147.6
$m_{MSD\parallel}/m_{MSD\perp}$	Anisotropy	73.0	92.0	56.0	39.0	33.0
IR	Frequency error	6.9	17.2	24.2	24.2	12.7
Riemannian distance	Minimal distance	6.8	24.8	0.0	13.5	8.3
Indentation modulus	$m = 19.75$ GPa	7.9	9.9	9.4	18.6	11.2
Total	Average error	36.1	37.6	38.7	37.8	36.3

flexible SPC is a reasonable choice for a classical water interaction potential.

However, Table 2 also makes clear that the accuracy of a specific property can vary significantly among water models. For this reason, the choice of water model can also depend greatly on the property of interest. Here, TIP5P water best predicted the Si–O bond stretching of infrared spectroscopy experiments; TIP3P best captured the structural predictions of X-ray diffraction experiments;

TIP4P exhibited the average density reported in experiments; and TIP4P05 well predicts the elastic constants. Therefore, one needs to choose a water model based on which characteristic is of interest. Thus, Table 2 provides one benchmark of water model selection based on the researchers' relative interest in structural, dynamic, and elastic properties of C–S–H.

4. Conclusions

To identify a sufficiently accurate and computationally efficient molecular water model for simulations of calcium–silicate–hydrate, we compared the structure, dynamics and mechanical properties of C–S–H calculated via five distinct, classical atomistic water models (SPC, TIP3P, TIP4P, TIP4P05, and TIP5P). We demonstrate that the choice of water model depends on the specific properties of interest and on the available computational resources. Moreover, we show that SPC (flexible) and TIP5P predict these C–S–H properties with comparable accuracy, and that SPC is more computationally efficient. This benchmarking and rational selection of classical water models can inform future simulations quantifying how the unique properties of water define and change the properties of cement.

References

[1] H.M. Jennings, Cement and Concrete Research 38 (2008) 275–289.
[2] F.A. Kirkpatrick, V.B. Orange, Journal of the American Ceramic Society 2 (1919) 44–64.
[3] H.N. Bordallo, L.P. Aldridge, A. Desmedt, Journal of Physical Chemistry B 110 (2006) 17966–17976.
[4] A.J. Allen, J.J. Thomas, H.M. Jennings, Nature Materials 6 (2007) 311–316.
[5] J.J. Beaudoin, R.F. Feldman, P.J. Tumidajski, Advanced Cement Based Materials 1 (1994) 224–236.
[6] I. Odler, Materials and Structures 24 (1991) 143–157.
[7] R.J.M. Pellenq, A. Kushima, R. Shahsavari, K.J. Van Vliet, M.J. Buehler, S. Yip, F.J. Ulm, PNAS 106 (2009) 16102–16107.
[8] F.X. Coudert, R. Vuilleumier, A. Boutin, ChemPhysChem 7 (2006) 2464–2467.
[9] C.J. Burnham, S.S. Xantheas, Journal of Chemical Physics 116 (2002) 5115–5124.
[10] A.V. Gubskaya, P.G. Kusalik, Journal of Chemical Physics 117 (2002) 5290–5302.
[11] M. Boero, K. Terakura, T. Ikeshoji, C.C. Liew, M. Parrinello, Physical Review Letters 85 (2000) 3245–3248.
[12] J.K. Gregory, D.C. Clary, K. Liu, M.G. Brown, R.J. Saykally, Science 275 (1997) 814–817.
[13] S.A. Clough, Y. Beers, G.P. Klein, L.S. Rothman, Journal of Chemical Physics 59 (1973) 2254–2259.
[14] G. Tammann, V. Jessen, Zeitschrift Fur Anorganische Und Allgemeine Chemie 179 (1929) 125–144.
[15] J.D. Bernal, R.H. Fowler, Journal of Chemical Physics 1 (1933) 515–548.
[16] B. Guillot, Journal of Molecular Liquids 101 (2002) 219–260.
[17] K. Szalewicz, C. Leforestier, A. van der Avoird, Chemical Physics Letters 482 (2009) 1–14.
[18] O. Teleman, B. Jonsson, S. Engstrom, Molecular Physics 60 (1987) 193–203.
[19] W.L. Jorgensen, J. Chandrasekhar, J.D. Madura, R.W. Impey, M.L. Klein, Journal of Chemical Physics 79 (1983) 926–935.
[20] W.L. Jorgensen, J.D. Madura, Molecular Physics 56 (1985) 1381–1392.
[21] J.L.F. Abascal, C. Vega, Journal of Chemical Physics 123 (2005) 234505–234515.
[22] M.W. Mahoney, W.L. Jorgensen, Journal of Chemical Physics 112 (2000) 8910–8922.
[23] R. Shahsavari, R.J.M. Pellenq, F.-J. Ulm, Physical Chemistry Chemical Physics 13 (2011) 1002–1011.
[24] H. Bekker, H.J.C. Berendsen, E.J. Dijkstra, S. Achterop, R. Vondrumen, D. Vanderspoel, A. Sijbers, H. Keegstra, B. Reitsma, M.K.R. Renardus, Physics Computing 92 (1993) 252–256.
[25] H.J.C. Berendsen, D. Vanderspoel, R. Vandrunen, Computer Physics Communications 91 (1995) 43–56.
[26] T. Kitamura, K. Yashiro, R. Ohtani, JSME International Journal. Series A-Solid Mechanics and Material Engineering 40 (1997) 430–435.
[27] F.M. Capaldi, M.C. Boyce, G.C. Rutledge, Journal of Chemical Physics 124 (2006) 214709–214713.
[28] P. Pavlides, D. Pugh, K.J. Roberts, Acta Crystallographica Section A 47 (1991) 846–850.
[29] R.A. Olson, H.M. Jennings, Cement and Concrete Research 31 (2001) 351–356.
[30] J.J. Thomas, H.M. Jennings, A.J. Allen, Journal of Physical Chemistry C 114 (2010) 7594–7601.
[31] J.J. Thomas, H.M. Jennings, Cement and Concrete Research 36 (2006) 30–38.
[32] M. Nilsson, J. Carlson, E. Fernandez, J.A. Planell, Journal of Material Science-Material in Medicine 13 (2002) 1135–1141.
[33] H. Manzano, R. Gonzalez-Teresa, J.S. Dolado, A. Ayuela, Materials for Construction 60 (2010) 7–19.
[34] C.F. Macrae, I.J. Bruno, J.A. Chisholm, P.R. Edgington, P. McCabe, E. Pidcock, L. Rodriguez-Monge, R. Taylor, Journal of Applied Crystallography 41 (2008) 466–470.
[35] H. Kim, W. Sigmund, Journal of Crystal Growth 267 (2004) 738–744.
[36] J. Houston, R. Maxwell, S. Carroll, Geochemical Transactions 10 (2009) 1–6.
[37] C. Vega, J.L.F. Abascal, M.M. Conde, J.L. Aragones, Faraday Discussions 141 (2009) 251–276.
[38] S.W. Rick, Journal of Chemical Physics 120 (2004) 6085–6093.
[39] Y. Ping, R.J. Kirkpatrick, P. Brent, F.M. Paul, C. Xiandong, Journal of the American Ceramic Society 82 (1999) 742–748.
[40] W. Humphrey, A. Dalke, K. Schulten, Journal of Molecular Graphics 14 (1996) 33–38.
[41] N. Malikova, A. Cade, V. Marry, E. Dubois, P. Turq, J.M. Zanotti, S. Longeville, Chemical Physics 317 (2005) 226–235.
[42] M. Gombia, V. Bortolotti, B. De Carlo, R. Mongiorgi, S. Zanna, P. Fantazzini, Journal of Physical Chemistry B 114 (2010) 1767–1774.
[43] A.G. Kalinichev, J.W. Wang, R.J. Kirkpatrick, Cement and Concrete Research 37 (2007) 337–347.
[44] S. Kamali-Bernard, F. Bernard, W. Prince, Computational Materials Science 45 (2009) 528–535.
[45] S. Bejaoui, B. Bary, Cement and Concrete Research 37 (2007) 469–480.
[46] R.F. Feldman, P. Sereda, Engineering Journal 8 (1999) 53–59.
[47] P. Colombet, A.R. Grimmer, H. Zanni, P. Sozzani, Nuclear magnetic resonance spectroscopy of cement-based materials Part II, Springer-Verlag, Berlin, 1998.
[48] S.H. Lee, P.J. Rossky, Journal of Chemical Physics 100 (1994) 3334–3345.
[49] N. Giovambattista, P.J. Rossky, P.G. Debenedetti, Physical Review E 73 (2006) 041604–041614.
[50] M. Vandamme, F.-J. Ulm, PNAS 106 (2009) 10552–10557.
[51] M.J. DeJong, F.-J. Ulm, Cement and Concrete Research 37 (2007) 1–12.
[52] C.A. Jones, Z.C. Grasley, Cement and Concrete Composites 33 (2011) 12–18.
[53] R. Alizadeh, J.J. Beaudoin, L. Raki, Materials and Structures 44 (2011) 13–28.
[54] F.-J. Ulm, M. Vandamme, C. Bobko, J. Alberto Ortega, K. Tai, C. Ortiz, Journal of the American Ceramic Society 90 (2007) 2677–2692.
[55] G. Constantinides, F.-J. Ulm, Journal of the Mechanics and Physics of Solids 55 (2007) 64–90.